Exploring the Potential of Multi-Substituted Hydroxyapatite: Sol-Gel Synthesis, Characterization, and *In Vitro* Biocompatibility Study

Sonia Sharma[1], Parveen Goyal[2,*], Dinesh Kumar[3,#]

[1]Dr. SSBUICET, Panjab University, Panjab University, Sector 14, Chandigarh, U.T. - 160014, India

[2]Mechanical Engineering, UIET, Panjab University, Chandigarh, U.T. - 160014, India

[3]University Centre for Research and Development, Chandigarh University, Mohali, Punjab, 140413, India

*,#Authors to whom any correspondence should be addressed:

Abstract: Calcium phosphates (CaPs) exist in various amorphous and crystalline forms, each with a different Ca/P molar ratio ranging from 0.5 for monocalcium phosphate monohydrate to 2 for tetracalcium phosphate. In this work, CaPs, hydroxyapatite (HA), have been studied for applications such as bone tissue engineering, orthopedic and dental implant coating, restoration of periodontal defects, and drug delivery systems due to their great similarity to the biological apatite. Out of all calcium phosphates, HA is most stable, most dense, and most insoluble. HA exists in two forms, namely monoclinic and hexagonal. The nano-dimensional HA and multi-substituted HA (with ions Sr, Mg, K, Zn, Mg) powders have been synthesized using water based sol-gel method. X-ray fluorescence spectroscopy (XRF) was used for the compositional analysis, BET analysis for the surface area, X-ray diffraction (XRD) for determining the purity, crystallinity, lattice parameters, and phase transformations, and Fourier Transform Infrared Spectroscopy (FTIR) for detecting functional groups. *In-vitro* study has been performed by immersing nanopowders in Silica-Bond-Fermatoxyl (SBF) for 30 days at 37°C. In-vitro studies confirmed the bioactive behavior of all as-synthesized and calcined nanopowders.

Keywords: Hydroxyapatite (HA), Multi-substituted Hydroxyapatite (MHA), Sol-gel technique, XRF, XRD, Fourier Transform Infrared Spectroscopy (FTIR), Bioactivity.

1. Introduction

Calcium phosphates (CaPs) occur in various forms, including monoclinic and hexagonal, with different Ca/P molar ratios[1]. Hydroxyapatite (HA) is the more stable, dense, and insoluble of all CaPs', with applications in bone tissue engineering, orthodontic and dental implant coating, periodontal defects restoration, and drug delivery systems[2]. Ionic substitution in HA is crucial as it affects bio-mineralization processes, properties of the precipitated phase, and increases the material's bioactivity[3]. Various cations or anions can be substituted into the HA structure due to its high structural stability and flexibility[4][5]. These substitutions play a vital role in the chemical composition, structure, surface, physical, chemical properties, and thermal stability of HA[6][7]. Dry chemical methods involve solid-state reactions between calcium and phosphorus compounds, while wet chemical methods involve reactions in solutions or solvents, typically water, at ambient or elevated temperatures[8]. Potassium plays a vital role in influencing the bio mineralization process, while manganese-doped HA promotes osteoblast proliferation, metabolism, and differentiation[9][10]. Zinc-substituted HA has more bioactivity and antimicrobial properties than unsubstituted HA[11]. Magnesium plays a crucial role in maintaining bone health by inhibiting crystallization, reducing crystal size, and decreasing osteoblast-like cell proliferation[12][13].

In this study, nano-dimensional HA and multi-substituted HA are made using a water-based sol-gel method. The X-ray fluorescence spectroscopy (XRF) is used for compositional analysis[14]. BET analysis for surface area, X-ray diffraction (XRD) for purity, crystallinity, lattice parameters, and phase transformations, and FTIR for functional group detection[15][16]. All as-synthesized and calcined nanopowders

exhibited bioactive behavior in in-vitro studies.

2. Experimentation

The work focused on hydroxyapatite nanopowders through a combination of calcium nitrate tetrahydrate (CNT), potassium dihydrogen phosphate ($KH_2(PO_4)$), magnesium nitrate hexahydrate ($Mg(NO_3)_2.6H_2O$), strontium nitrate ($Sr(NO_3)_2$), zinc nitrate tetrahydrate ($Zn(NO_3)_2.4H_2O$), and potassium nitrate (KNO3) as precursors. The pH was maintained at 10±0.1 using a 25% NH4OH solution. The precursors were added dropwise to solution B, which was then stirred under vigorous mixing at 1100 rpm for 1 hour at $25^{O}C$. The hydroxyapatite structure's gelation and polymerisation were enhanced by adding 25% NH_4OH solution to the pH, which was continuously monitored and set to 10±0.1. After the gel was allowed to age for a full day, the gelatinous precipitates were separated by centrifugation and carefully cleaned with double-distilled, warm water[17][18]. The precipitates were crushed and pulverised into fine powders after being dried for 24 hours at 70°C in an oven. The as-synthesized nanopowder was designated as HA (Figure 1). Table 1 shows the Amount of precursors for the synthesis of hydroxyapatite nanopowder.

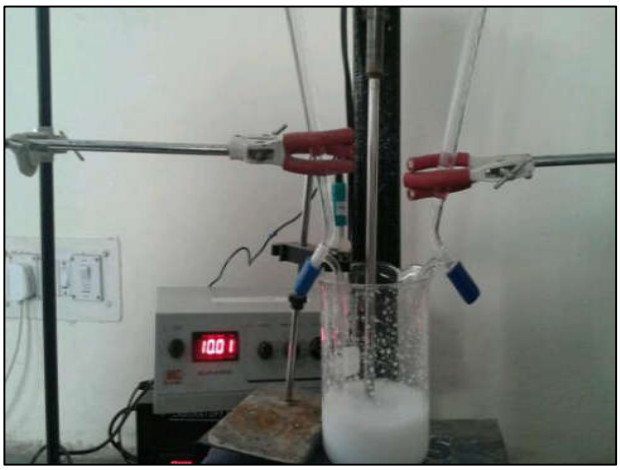

Figure 1: Experimental set of sol-gel synthesis

Table 1: Amount of precursors for the synthesis of hydroxyapatite nanopowder

Precursor	Moles of Precursor added	Molecular weight of precursor	Quantity of precursor added for 1M solution (1 liter)	Quantity of precursor added for 1M solution (500 ml)
CNT	1	236.15	236.15	118.075
KDP	0.6	136.08	81.648	40.824

The synthesis of hydroxyapatite nanopowder ($Ca_{10}(PO_4)_6(OH)_2$) involved the preparation of two solutions: solution A, which contained calcium nitrate tetrahydrate, magnesium nitrate hexahydrate, strontium nitrate, zinc nitrate tetrahydrate, and potassium nitrate, and solution B, which contained potassium dihydrogen phosphate (KDP). The precursors were mixed and added to solution B under vigorous stirring at 1100 rpm for 1 hour at room temperature. The pH was adjusted to 10±0.1 by adding 25% NH_4OH solution. The gel formed was aged for 24 hours, and the gelatinous precipitates were centrifuged and washed to remove ammonia. The precipitates were dried in an oven at 70°C for 24 hours, and the dried mass was crushed and ground to obtain fine powders. The as-synthesized nanopowder was designated as MHA (Table 2).

Table 2: Amount of precursors for the synthesis of MHA nanopowder

Precursor	Moles of precursor added	Molecular Weight of precursor	Quantity of Precursor Added for 1M Solution(1 liter)	Quantity of Precursor Added for 1M Solution(500 ml)
CNT	1.7395	236.16	182.2135	91.067
MNH	0.3	256.41	34.119	17.059
SN	0.025	211.63	2.346	1.173
ZNT	0.01	261.44	1.159	0.579
KN	0.03	101.10	1.3453	0.6726
KDP	1.35	136.08	81.4850	40.9225

The study focuses on the elemental analysis of nanopowders using energy-dispersive - XRD (ED-XRF). With the use of a hydraulic press, a 34 mm diameter and 1.5 mm thickness nanopowder pellet was produced. By estimating the relative quantities of various phases, the Brunauer-Emmett-Teller approach evaluated the BET surface area[19]. XRD was performed on the nanopowders using CuKα radiation. The fraction of phases formed was determined using XRD data, and using Scherer's equation, the crystallite size of the nanopowders was determined[20][22]. Three highly intensified peaks in the XRD spectra were used to determine the mean crystallite size of the as-synthesised nanopowders. For calcined nanopowders, three diffraction peaks (002), (112), and (300) were chosen. We used the following equation to compute the cell parameters, a and c: Phase of β-TCP and HA: 1/d^2 = 4/3. In the α-TCP phase, 1/d^2 = h^2/a^2 + h^2/b^2 + l^2/c^2 (orthogonal) and (h^2+k^2+hk)/a^2 +l^2/c^2 (hexagonal). KBr pellets (1% wt/wt) were used to record infrared spectra in the 400–4000 cm-1 range, with a spectral resolution of 2 cm-1 for the nanopowders. Analysing the spectra allowed us to determine which functional groups—such as hydroxyl, phosphates, nitrates, and carbonates—were present in the nanopowders. SBF (Silica-Bond-Fermatoxyl) was prepared by heating a 1000 ml beaker with 700 ml of distilled and ion-exchanged water to 36.5 ± 1.5°C, then adding reagents 1-7 one at a time. The pH of the simulated body fluid was adjusted using the reagents 8th and 9th. Thus the study aims to understand the properties of nanopowders and their potential applications in various fields. The use of ED-XRF, XRD, and FTIR techniques was employed to analyze the nanopowders and their potential applications in various industries. Reagents were mixed and then dissolved one after the other until SBF was ready. The volume of 1M-HCl was measured after a 1M-HCl wash. It was easy to test hygroscopic reagents such as KCl, $K_2HPO_4.3H_2O$, $MgCl_2.6H_2O$, $CaCl_2$, and Na_2SO_4. If the quantity was less than 900 ml, distilled water was added, and the solution temperature was adjusted to 36.5 ± 1.5°C. Tris was dissolved after the solution's pH was kept at 2.0 ± 1.0. Table 3 shows the chemicals used for the preparation of SBF.

Table 3: Chemicals used for the preparation of SBF.

S. No.	Reagents for SBF	Amount used (1000 ml)
1.	NaCl	8.035 gm
2.	$NaHCO_3$	0.355 gm
3.	KCl	0.225 gm
5.	$CaCl_2$	0.292 gm
6.	$MgCl_2.6H_2O$	0.311 gm
7.	Na_2SO_4	0.072 gm
8.	$(HOCH_2)_3CNH_2$	6.118 gm
9.	HCl (1M)	39 ml

Reagent Tris, which was progressively added to keep the temperature between 35°C

and 38°C, was used to monitor the pH of a solution. We first adjusted the pH to 7.30 ± 0.05 and then added additional Tris to get it down to 7.45. When the pH hit 7.45 0.01, the addition of Tris was stopped, and 1M-HCl was added to bring the pH down to 7.42 0.01, making sure it did not go below 7.40. If Tris was still present, 1M-HCl and Tris were added in turns until the pH became less than 7.45. We next lowered the temperature of the solution to 36.5 ± 0.2°C. Add 1M-HCl dropwise until the pH reached 7.42 ± 0.01 at 36.5 ± 0.2°C, and then exactly 7.40 at 36.5°C. After removing the electrode from the pH meter, distilled, ion-exchanged water was used to wash and rinse the mixture. The pH-adjusted solution was poured into a 1000 ml volumetric flask, and the stirring bar was fixed in place using a magnet. We added distilled and ion-exchanged water to the flask, stirred the mixture, and let it cool in water to 20°C. When the temperature of the solution dropped to 20°C, distilled water was once again added.

Results and discussion

The amount of potassium, zinc, magnesium, strontium substituted in MHA was less as compared to the amount in preparatory solution as shown in table 4. In as-synthesized HA nanopowder, the obtained Ca/P ratio was greater than the stoichiometric ratio (1.67). The Ca/P ratio greater than 1.67 showed the formation of amorphous calcium phosphate (ACP). In ACP, Ca/P ratio varies from 1.2-2.2.

Table 4: Elemental composition of as-synthesized HA and MHA nanopowders

Elements Substituted	Nanopowder Composition in moles	
	HA	MHA
	As-Synthesized	As-Synthesized
Ca	1.7257	1.2898
P	0.99502	1.30125
Sr	0	0.000177
K	0	0.01626
Zn	0	0.000599
Mg	0	0.28065
(Ca+M)/P	1.73402	1.21997

Table 5 shows the BET surface area of as-synthesized and calcined HA and MHA. As-synthesized HA powder had lager area as compared to the as-synthesized MHA nanopowder.

Table 5: BET Surface area of as-synthesized and calcined HA and MHA nanopowders.

BET surface area (m^2/gm)			
Nanopowder	As-synthesized	Calcined	
		800˚C	1000˚C
HA	114.50	15.60	1.42
MHA	112.82	15.37	1.36

The study found that as temperature increased, the surface area of the powder decreased due to the increase in particle size, primarily due to the calcination effect within the powder particles.

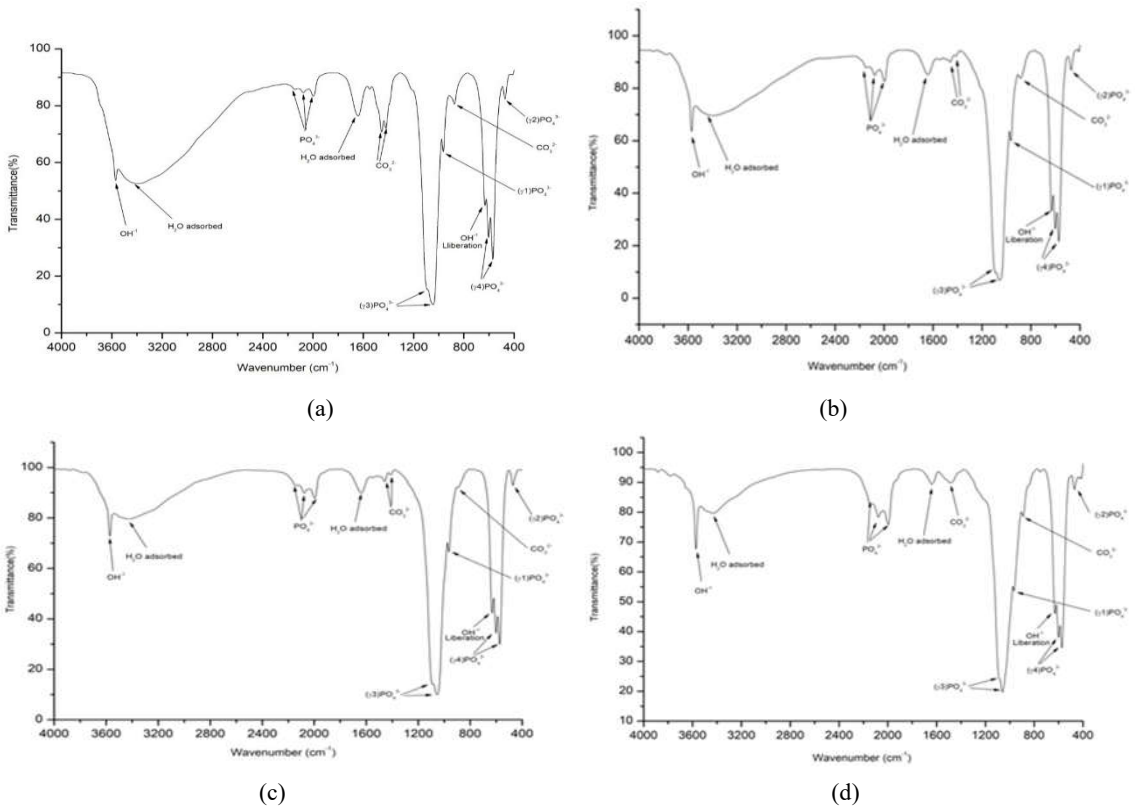

Figure 2: FTIR spectrum of as-synthesized HA, HA8, HA10, HA12 nanopowder

Figure 2(a) shows the IR spectra of the as-synthesized HA nanopowder. The spectra showed the absorption bands related to the modes of: phosphate (ν_1 symmetric stretch, 963.5 cm^{-1}; ν_2 bending, 473.1 cm^{-1}; ν_3 asymmetric stretch, 1089.1 cm^{-1}, 1044.5 cm^{-1}; ν_4 bending, 603.2 cm^{-1} and 570 cm^{-1}), hydroxyl (stretching 3596.6 cm^{-1}; librational mode (632.3 cm^{-1}), adsorbed water (bending, 1641.2 cm^{-1}; symmetric + asymmetric stretch, 3397.6 cm^{-1}), carbonate in B position (bending, 876.1cm^{-1}; stretching,1453.3 cm^{-1}, 1420 cm^{-1}). Weak intensity absorption connected with combination of ν_3, ν_4 of phosphate (2075.9 cm^{-1}, 1996.1 cm^{-1} and were present at 2152.2 cm^{-1}. Figure 2(b) shows the IR spectra of HA8 nanopowder. It showed the absorption bands related to the modes of: phosphate (ν_1 symmetric stretch, 965 cm^{-1}; ν_2 bending, 470;9 cm^{-1}; ν_3 asymmetric stretch, 1091.4 cm^{-1}, 1054.7 cm^{-1}; ν_4 bending, 602.3 cm^{-1} and 572.6 cm^{-1}), hydroxyl (stretching 3570.8 cm^{-1}; librational mode (632.1 cm^{-1}), adsorbed water bending, 1642.4 cm^{-1}; symmetric+asymmetric stretch, 3402.9 cm^{-1}), carbonate in B position (bending, 887.3 cm^{-1}; stretching, ~1459.9 cm^{-1}, 1414.2 cm^{-1}). Weak intensity absorption connected with combination of ν_3, ν_4 of phosphate were present at 2076.9 cm^{-1}, 1995.1 cm^{-1} and 2151.9 cm^{-1}.
Figure 2(c) shows the IR spectra of the HA10 nanopowder. It showed the absorption bands related to the modes of: phosphate (ν_1 symmetric stretch, 964.2 cm^{-1}; ν_2 bending, 470.5 cm^{-1}; ν_3 asymmetric stretch, 1091.5 cm^{-1}, 1053.8cm^{-1}; ν_4 bending, 602.2 cm^{-1} and 572.8 cm^{-1}), hydroxyl (stretching 3571 cm^{-1}; librational mode (631.9 cm^{-1}), adsorbed water bending, 1638.1 cm^{-1}; symmetric+asymmetric stretch, 3422.3 cm^{-1}), carbonate in B position (bending, 888.7 cm^{-1}; stretching, 1459.9 cm^{-1}, 1441.4 cm^{-1}). Weak intensity absorption connected with combination of ν_3, ν_4 of phosphate were present at 2075.8 cm^{-1}, 1995.1 cm^{-1} and 2150.2 cm^{-1}.

Figure 2(d) shows the IR spectra of the HA12 nanopowder. It showed the absorption bands related to the modes of: phosphate (ν_1 symmetric stretch, 965.7 cm^{-1}; ν_2 bending, 469.6 cm^{-1}; ν_3 asymmetric stretch, ~1090.7 cm^{-1}, 1060.3cm^{-1}; ν_4 bending, 600.5 cm^{-1} and 573.5 cm^{-1}), hydroxyl (stretching ~3571.7 cm^{-1}; librational mode (630.7 cm^{-1}), adsorbed water bending, ~1637.4 cm^{-1}; symmetric+asymmetric stretch, 3433.7 cm^{-1}), carbonate in B position (bending, 890.9cm^{-1}; stretching, 1488.1 cm^{-1}). Weak intensity absorption connected with combination of ν_3, ν_4 of phosphate were

present at 2075.9, 1994.9 and 2151.4 cm^{-1}.

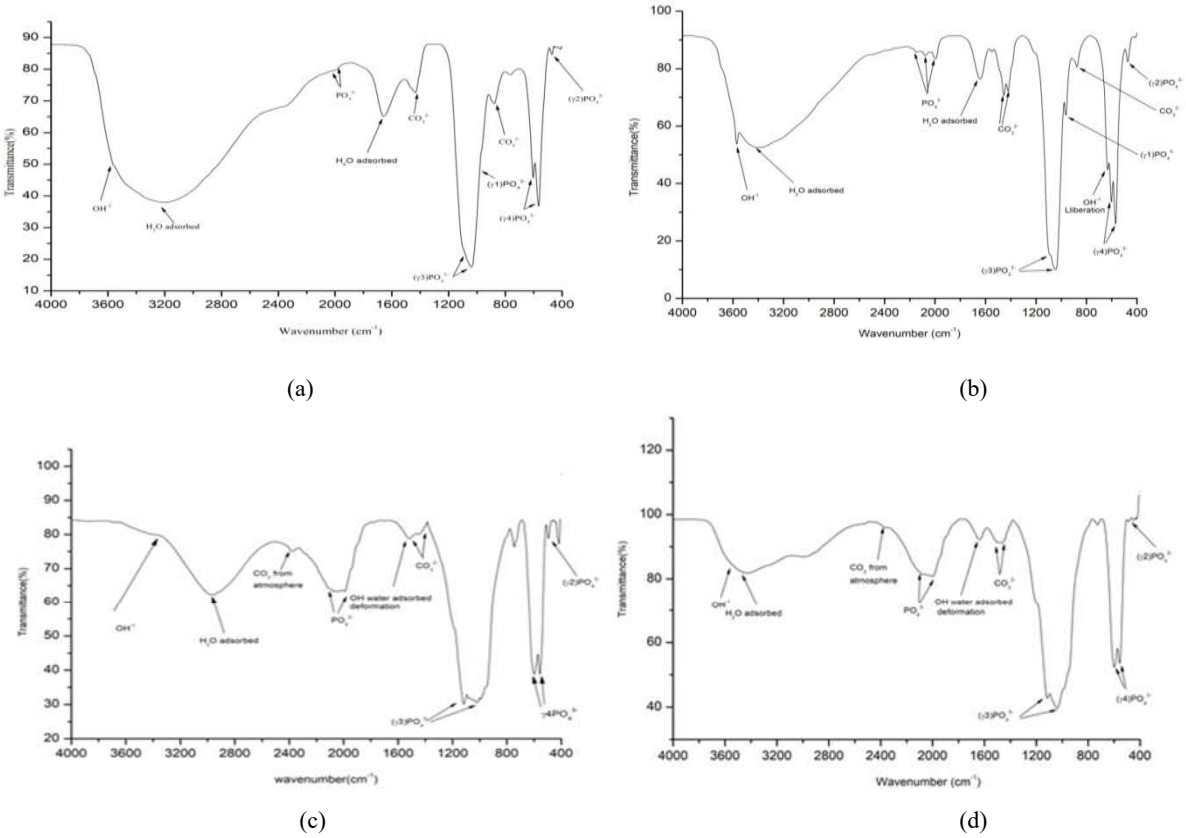

Figure 3: FTIR spectrum of MHA nanopowder

Figure 3(a) shows the IR spectra of the as-synthesized MHA nanopowder. It showed the absorption bands related to the modes of: phosphate (ν_1 symmetric stretch, 966 cm^{-1}; ν_2 bending, 470.8 cm^{-1}; ν_3 asymmetric stretch, 1082.3 cm^{-1}, 1039.5 cm^{-1}; ν_4 bending, 604.3 cm^{-1} and 565.3 cm^{-1}), hydroxyl (stretching 3569.65 cm^{-1}; adsorbed water bending, 1658 cm^{-1}; symmetric+asymmetric stretch, 3169 cm^{-1}), carbonate in B position (bending, 877.6 cm^{-1}; stretching, 1433.2 cm^{-1}). Weak intensity absorption connected with combination of ν_3, ν_4 of phosphate ware present at 2014.1 cm^{-1} and 1979.9 cm^{-1}.

Figure 3(b) shows the IR spectra of MHA8 nanopowder. It showed the absorption bands related to the modes of: phosphate (ν_1 symmetric stretch, 964.5 cm^{-1}; ν_2 bending, 488.7 cm^{-1}; ν_3 asymmetric stretch, 1088.5 cm^{-1}, 1051.4 cm^{-1}; ν_4 bending, 602.7 cm^{-1} and 560 cm^{-1}), hydroxyl (stretching 3571.9 cm^{-1}; adsorbed water bending, 1679.9 cm^{-1}; symmetric+asymmetric stretch, 2987.2 cm^{-1}), carbonate in B position (bending, 891.6 cm^{-1}; stretching, 1513.5 cm^{-1}, 1406.5 cm^{-1}). Weak intensity absorption connected with combination of ν_3, ν_4 of phosphate were present at 2075.9 cm^{-1} and 1990.2 cm^{-1}.

Figure 3(c) shows the IR spectra of the MHA10 nanopowder. It showed the absorption bands related to the modes of: phosphate (ν_2 bending, 493 cm^{-1}; ν_3 asymmetric stretch, 1117.8 cm^{-1}, 1020.8cm^{-1}; ν_4 bending, 602.2 cm^{-1} and 558 cm^{-1}), hydroxyl (stretching 3555 cm^{-1}; adsorbed water bending, ~1658.9 cm^{-1}; symmetric+asymmetric stretch, 2957.3 cm^{-1}), carbonate in B position (bending, ~888.7 cm^{-1}; stretching, 1512 cm^{-1}, 1413 cm^{-1}).Weak intensity absorption connected with combination of ν_3, ν_4 of phosphate were present at 2042.5 $cm^{-1}$and 1991.1cm^{-1}.

Figure 3(d) shows the IR spectra of the MHA12 nanopowder. It showed the absorption bands related to the modes of: phosphate (ν_1 symmetric stretch, ~978.6 cm^{-1}; ν_2 bending, ~486.2 cm^{-1}; ν_3 asymmetric stretch, 1144.6. cm^{-1}, 1039.8 cm^{-1}; ν_4 bending, 599 cm^{-1} and 557.2 cm^{-1}), hydroxyl (stretching 3508.5 cm^{-1}; adsorbed water bending, ~1637 cm^{-1}; symmetric+asymmetric stretch, 3417 cm^{-1}), carbonate

in B position (bending, ~890.9 cm^{-1}; stretching, 1464, 1514 cm^{-1}). Weak intensity absorption connected with combination of ν_3, ν_4 of phosphate were present at 1997.8 cm^{-1}, 2098 cm^{-1}.

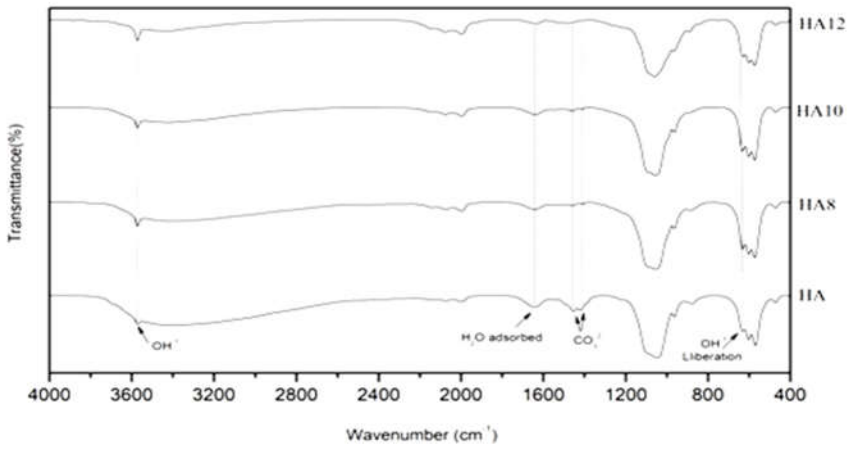

Figure 4: Comparison of FTIR spectra of HA, HA8, HA10 and HA12 nanopowders

Figure 4 shows that water adsorption band nearly disappeared with calcination of as-synthesized HA. However, the sharp peaks at 3570 & 630 cm^{-1} referred to the variations of structural OH^- group, which is characteristic to structure of HA. The thermal treatment of the nanopowder at 800˚C, 1000˚C & 1200˚C eliminated the CO_3^{2-} concentration in the as-synthesized powder.

It is evident from the illustration (Figure 5) that calcination of the as-synthesized MHA at 1200˚C narrowed the water adsorption band. The sharp peaks at 3570 and 630 cm^{-1} referred to the variations of structural OH^- group, which was characteristic to structure of HA. The thermal treatment of the nanopowder at 800˚C, 1000˚C & 1200˚C eliminated the CO_3^{2-} concentration in the as-synthesized powder.

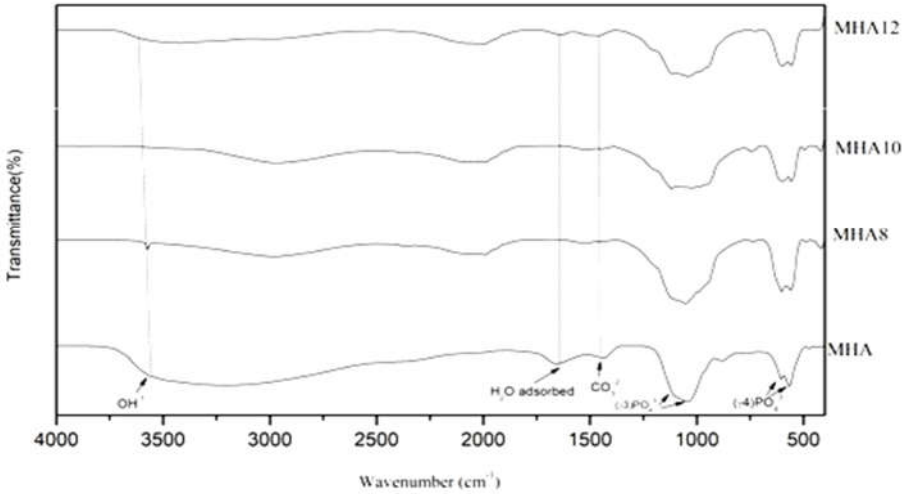

Figure 5: Comparison of FTIR spectra of MHA, MHA8, MHA10, and MHA12 nanopowders

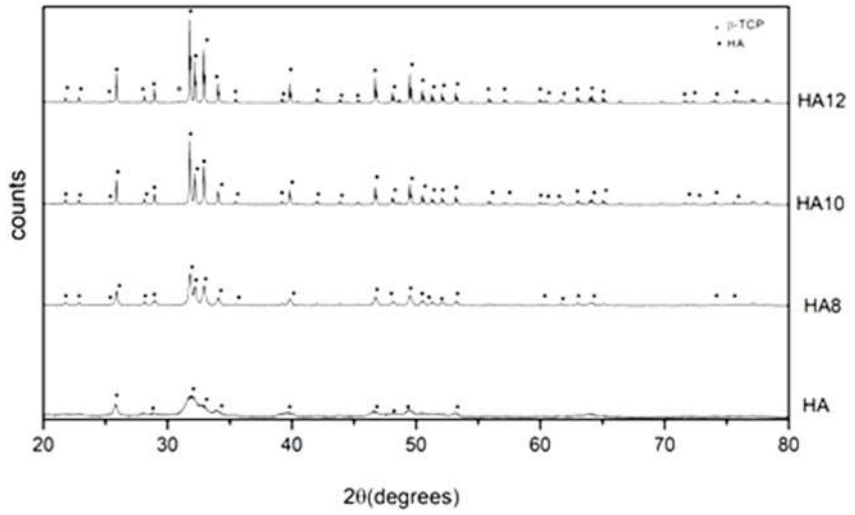

Figure. 6: Comparison of XRD pattern of as-synthesized and calcined HA nanopowders.

Figure 6 shows the comparison of XRD patterns of as-synthesized HA, HA8, HA10 and HA12 nanopowders. The as-synthesized nanopowders showed broad diffraction pattern which means low crystallinity of as-synthesized nanopowder. The as-synthesized sample had pure HA phase. On calcination of as-synthesized powder at 800 and 1000˚C, no secondary phase was observed. β-TCP was observed as minor phase when calcination was done at 1200˚C. In HA12 nanopowder, major phase was HA. From table 6 it was observed that with the increase of temperature, the crystallinity increased from 10.13% to 98.01%. The mean crystallite size with respect to HA phase tend to increase from 17.23 nm for as-synthesized nanopowder to 143.32 nm for HA12 nanopowder (Table 7).

X-ray diffraction (XRD) patterns of as-synthesized and calcined HA nanopowders (Figure 6). XRD patterns of all as-synthesized nanopowders i.e. HA and MHA matched with the JCPDS data of HAP and β-TCP (JCPDS card numbers 09-0432 and 09-0169). The substitution of ions viz. Mg^{2+}, Sr^{2+}, K^{+} and Zn^{2+} did not affect the diffraction pattern. Secondary phase such as β-TCP or α-TCP appeared on calcination at 800˚C and above.

X-ray diffraction (XRD) patterns of as-synthesized and calcined MHA nanopowders (calcined at 800˚C, 1000˚C and 1200˚C, respectively). The as-synthesized MHA is calcium-deficient hydroxyapatite with Ca/P molar ratio less than 1.67, HA being the primary phase and no other secondary phase. However, calcination of the powder at different temperatures transformed it to biphasic or triphasic mixture with different compositions of HA, β and α phases depending on the calcination temperature.

Figure 7 shows the comparison of XRD patterns of as-synthesized MHA, MHA8, MHA10, and MHA12 nanopowders. The as-synthesized nanopowder showed a broad diffraction pattern, which means low crystallinity of nanopowders. The as-synthesized nanopowder had pure HA phase, which transformed to β-TCP and α-TCP phase on calcination at 800˚C, with α-TCP phase in highest quantity, unlike pure HA calcined at the same temperature. The calcination from 800˚C to 1000˚C increased the composition of β phase and α phase. However, the transformation was not significant at 1200˚C with α-TCP, the primary phase constituting nearly 53.46% of the total composition. The mean crystallite size with respect to HA phase tends to increase from 17.48 nm for as-synthesized MHA nanopowder to 89.76 nm for MHA12 nanopowder. Table 8 shows the composition of as-synthesized and calcined MHA nanopowders.

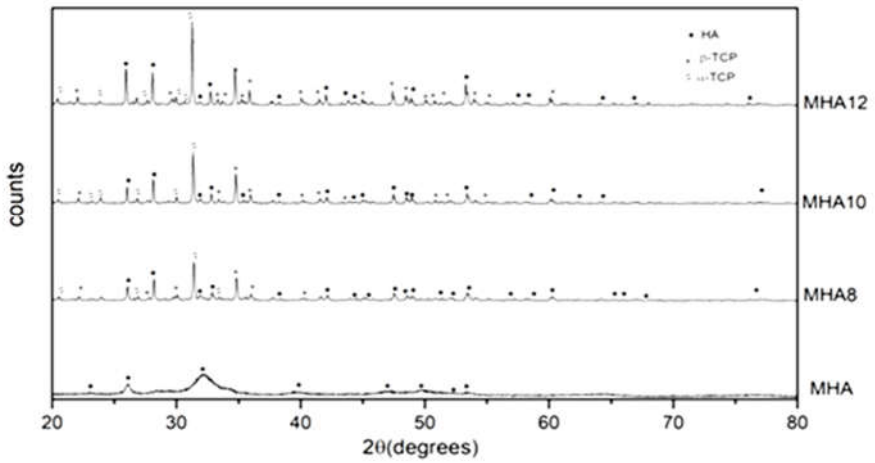

Figure 7: Comparison of XRD patterns of as-synthesized and calcined MHA nanopowders

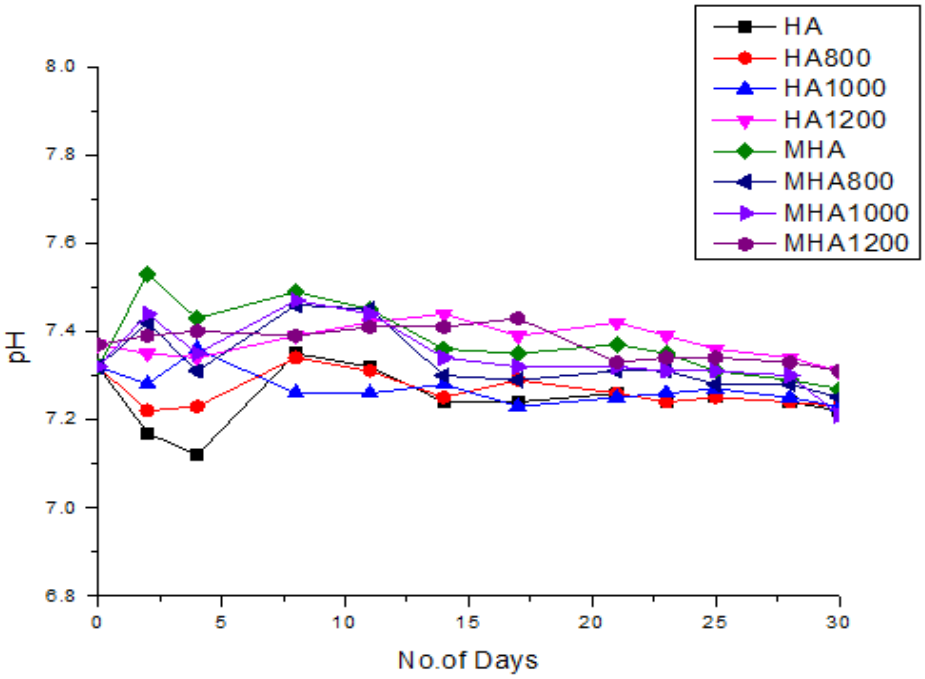

Figure 8: pH change in SBF with time of immersion for as-synthesized and calcined HA and MHA nanopowders

Table 6: Composition of as-synthesized and calcined HA nanopowders

Nanopowder	% Crystallinity	Composition (wt. %)		
		% HA	% β-TCP	% α-TCP
HA	10.13	100	0	0
HA8	85.17	100	0	0
HA10	97.06	100	0	0
HA12	98.01	96.12	3.88	0

Table 7: Calculated cell parameters for as- synthesized and calcined HA nanopowder

Nanopowder	Lattice parameters (Å)			Mean crystallite size (nm)	Unit cell volume (Å)^3	
	% HA a=b, c	% β-TCP a=b, c	% α-TCP a= b= c=		HA phase $V=3*a^2*c$	β-TCP phase $V=0.866*a^2*c$
HA	a= 9.4418 c= 6.8895	0 0	0 0 0	17.23	1842.546	0
HA8	a= 9.427 c=6.891	0 0	0 0	59.224	1837.174	0
HA10	a= 9.434 c=6.896	0 0	0 0 0	110.048	1837.239	0
HA12	a= 9.437 c=6.891	a= 10.416 c=37.362	0 0 0	143.32	1841.074	3510.449

Table 8: Composition of as-synthesized and calcined MHA nanopowders

Nanopowder	% Crystallinity	Composition (wt %)		
		% HAP	% β-TCP	% α-TCP
MHA	9.979	100	0	0
MHA8	79.40	26.41	27.06	46.53
MHA10	87.50	22.509	28.191	49.30
MHA12	91.47	23.35	23.19	53.46

Table 9: Calculated cell parameters for as-synthesized and calcined HA nanopowders

Nanopowder	Lattice parameters (Å)			Mean crystallite size (nm)	Unit cell volume(Å)^3		
	% HAP a=b, c	% β-TCP a=b, c	% α-TCP a= b= c=		HAP phase	β-TCP phase	α-TCP phase
MHA	a= 9.441 c= 6.881	0 0	0 0	17.48	1840.214	0	0
MHA8	a= 9.411 c=6.889	a= 10.37 c=37.165	a=15.335 b=20.951 c=8.951	51.234	1830.412	3467.175	2875.809
MHA10	a= 9.421 c=6.862	a= 10.38 c=37.525	a=15.443 b=20.965 c=8.968	71.8283	1832.52	3506.5	2903.502
MHA12	a= 9.431 c=6.883	a= 10.39 c=37.597	a=15.432 b=20.976 c=9.012	89.76	1836.599	3520.33	2917.199

Table 9 shown the calculated cell parameters for as- synthesized and calcined HA nanopowders. Substitution of Mg^{2+} and Zn^{2+} in HA lattice decreased the thermal stability and decreased the phase transformation temperature. Whereas substitution of Sr^{2+} and K^{+} increases stability and increases the phase transformation temperatures. From Table 1, it was seen that highest substituted ion is magnesium due to this the phase transformation temperature decreased for MHA, hence forth allowing the synthesis of α-TCP phase at much lower temperature (800˚C). From

this, it is evident that the incorporation of ions reduced the thermal stability of MHA.The bioactivity behavior of the nanopowders was analyzed by immersing nanopowders in change of SBF for simulated body fluid for 30 days at 37˚C as shown in Figure 8. The change in pH of all the synthesized and calcined nanopowders was recorded after a gap of 48 hours continuously for a month. It was observed that the pH keeps on decreasing and increasing alternately throughout the period of in-vitro study and the pH generally changes regularly in increasing and decreasing manner, showing bioactive behaviour of nanopowders. The decrease of pH in SBF is directly proportional to the calcium consumption.

$PO\text{-}H + Ca^{2+} \rightarrow (PO)_2Ca + 2H^+$

The solubility of the apatite rises with H^+ion concentration, suggesting the dissolution of the surface layer, and this reaction would cause a fall in pH. It was observed that HA, HA8, HA10, and HA12 nanopowder samples showed an initial decrease of pH value, and afterwards, the pH value increased and decreased alternatively. The initial decrease in pH was highest for HA and least for HA12. This behavior continued till the period of the present investigation of 30 days. On the other hand, MHA, MHA8, MHA10, and MHA12 nanopowder samples showed the initial increase of pH value and afterwards, the pH value decreased and increased alternatively. The initial increase in pH was highest for HA and least for MHA12. This behavior continued till the period of the present investigation of 30 days.

Conclusions

The important outcomes of the present study are given below:

1. Nano dimensional powders of HA and MHA were successfully synthesized by water based sol-gel technique. Potassium, magnesium, zinc and strontium substitution in hydroxyapatite was confirmed from XRF spectra; however, their concentrations were lower than the corresponding initial concentrations in preparatory solutions used for synthesis.
2. As indicated from XRD patterns, all as-synthesized nanopowders possessed hydroxyapatite phase, which matched well with JCPDS card no. 09-432. On calcination of HA, very small amount of hydroxyapatite transformed to β-TCP. But on calcination of MHA nanopowder, large amount of hydroxyapatite phase transformed to β-TCP and α-TCP.
3. All as-synthesized nanopowders were amorphous in nature. The crystallinity increased with calcination temperature from 800°C to 1200°C for all nanopowders. It was between 85-98% and 87-91% for calcined HA and MHA nanopowders, respectively.
4. The mean crystallite size of as-synthesized HA and MHA nanopowders as calculated from XRD data were in the nano range, 17-143 nm and 17-90 nm, respectively. The mean crystallite size of nanopowders increased with increase in calcination temperature.
5. The lattice parameters ‘a’ and ‘c’ of MHA nanopowder were smaller as compared to the HA nanopowder. This happened due to the substitution of smaller ions into hydroxyapatite lattice.
6. The FTIR spectrum of all as-synthesized and calcined nanopowders confirmed the characteristic peaks of pure hydroxyapatite. The peak of OH-1 in FTIR spectra of MHA as-synthesized and calcined nanopowders was smaller as compared to the HA as-synthesized and calcined nanopowders.
7. The in-vitro studies of all as-synthesized and calcined nanopowders confirmed the bioactive behavior of nanopowders.

The research can be expanded by using advanced AI applications and optimization techniques to improve the synthesis process and properties. Predictive models aid optimizing, synthesis of parameters, desired properties, and reduce experimental trials. Techniques like Taguchi can enhance material properties like crystallinity, bioactivity, and mechanical strength, ensuring consistent production.

References

[1] S. Gautam and P. Singhal, “Calcium Phosphate: Synthesis andApplications,” *Calcium-Based Mater. Process. Charact. Appl.*, pp. 5–25, Jan. 2024, doi: 10.1201/9781003360599-2.

[2] H. Zhou, L. Yang, U. Gbureck, S. B. Bhaduri, and P. Sikder, “Monetite, an important calcium phosphate compound–Its synthesis, properties and applications in orthopedics,” *Acta Biomater.*, vol. 127, pp. 41–55, Jun. 2021, doi: 10.1016/J.ACTBIO.2021.03.050.

[3] N. Ramesh, J. T. B. Ratnayake, and G. J. Dias, “Calcium-based ceramic biomaterials,” *Struct. Biomater. Prop. Charact. Sel.*, pp. 333–394, Jan. 2021, doi: 10.1016/B978-0-12-818831-6.00011-2.

[4] A. Ressler, A. Žužić, I. Ivanišević, N. Kamboj, and H. Ivanković, “Ionic substituted hydroxyapatite for bone regeneration applications: A review,” *Open Ceram.*, vol. 6, Jun. 2021, doi: 10.1016/J.OCERAM.2021.100122.

[5] G. Singh, R. P. Singh, and S. S. Jolly, “Customized hydroxyapatites for bone-tissue engineering and drug delivery applications: a review,” *J. Sol-Gel Sci. Technol.*, vol. 94, no. 3, pp. 505–530, Jun. 2020, doi: 10.1007/S10971-020-05222-1.

[6] S. Tabassum, “Role of substitution in bioceramics,” *Handb. Ion. Substituted Hydroxyapatites*, pp. 117–148, Nov. 2019, doi: 10.1016/B978-0-08-102834-6.00005-7.

[7] S. A. Siddiqi and U. Azhar, “Carbonate substituted hydroxyapatite,” *Handb. Ion. Substituted Hydroxyapatites*, pp. 149–173, Nov. 2019, doi: 10.1016/B978-0-08-102834-6.00006-9.

[8] N. A. S. Mohd Pu’ad, R. H. Abdul Haq, H. Mohd Noh, H. Z. Abdullah, M. I. Idris, and T. C. Lee, “Synthesis method of hydroxyapatite: A review,” *Mater. Today Proc.*, vol. 29, pp. 233–239, 2019, doi: 10.1016/J.MATPR.2020.05.536.

[9] Y. Luo *et al.*, “Metal ions: the unfading stars of bone regeneration—from bone metabolism regulation to biomaterial applications,” *Biomater. Sci.*, vol. 11, no. 22, pp. 7268–7295, Sep. 2023, doi: 10.1039/D3BM01146A.

[10] S. Muthusamy, B. Mahendiran, S. Sampath, S. N. Jaisankar, S. K. Anandasadagopan, and G. S. Krishnakumar, “Hydroxyapatite nanophases augmented with selenium and manganese ions for bone regeneration: Physiochemical, microstructural and biological characterization,” *Mater. Sci. Eng. C*, vol. 126, Jul. 2021, doi: 10.1016/J.MSEC.2021.112149.

[11] K. Ijaz, H. Khalid, and A. A. Chaudhry, “Zinc-substituted hydroxyapatite,” *Handb. Ion. Substituted Hydroxyapatites*, pp. 217–236, Nov. 2019, doi: 10.1016/B978-0-08-102834-6.00009-4.

[12] M. Nabiyouni, T. Brückner, H. Zhou, U. Gbureck, and S. B. Bhaduri, “Magnesium-based bioceramics in orthopedic applications,” *Acta Biomater.*, vol. 66, pp. 23–43, Jan. 2018, doi: 10.1016/J.ACTBIO.2017.11.033.

[13] S. K. Venkatraman and S. Swamiappan, “Review on calcium- and magnesium-based silicates for bone tissue engineering applications,” *J. Biomed. Mater. Res. - Part A*, vol. 108, no. 7, pp. 1546–1562, May 2020, doi: 10.1002/JBM.A.36925.

[14] V. K. Sharma, P. Kumar, S. Akhai, V. Kumar, and R. S. Joshi, “Corrosion inhibition analysis on cerium induced hydrophobic surface of Al-6061/SiC/Al2O3 hybrid composites,” *Proc. Inst. Mech. Eng. Part B J. Eng. Manuf.*, vol. 238, no. 14, pp. 2126–2138, Dec. 2024, doi: 10.1177/09544054231222048.

[15] A. S. Wadhwa and A. Chauhan, “An Overview of the Mechanical and Tribological Characteristics of Non-Ferrous Metal Matrix Composites for Advanced Engineering Applications,” *Tribol. Ind.*, vol. 45, no. 1, pp. 51–80, 2023, doi: 10.24874/TI.1359.08.22.12.

[16] A. S. Wadhwa and H. S. Dhaliwal, “A textbook of engineering material and metallurgy,” 2009.

[17] M. E. Atya, X. Yang, Y. Tashiro, R. Tuvikene, and S. Matsukawa, “Structural and physicochemical characterization of funoran extracted from Gloiopeltis furcata by different methods,” *Algal Res.*, vol. 76, Nov. 2023, doi: 10.1016/J.ALGAL.2023.103334.

[18] A. D. Khan, M. K. Singh, and P. M. Lavhale, “Polyherbal phytosomal gel for enhanced topical delivery: design, optimization by central composite design, in vitro and ex-vivo evaluation,” *J. Dispers. Sci. Technol.*, vol. 45, no. 6, pp. 1061–1074, 2024, doi: 10.1080/01932691.2023.2195927.

[19] Z. Gholizadeh, M. Aliannezhadi, M. Ghominejad, and F. S. Tehrani, “High specific surface area γ-Al2O3 nanoparticles synthesized by facile and low-cost co-precipitation method,” *Sci. Rep.*, vol. 13, no. 1, Dec. 2023, doi: 10.1038/S41598-023-33266-0.

[20] S. A. Hassanzadeh-Tabrizi, “Precise calculation of crystallite size of nanomaterials: A review,” *J. Alloys Compd.*, vol. 968, Dec. 2023, doi: 10.1016/J.JALLCOM.2023.171914.